

# Unified model for describing the evolution of negative capacitance in perovskite solar cells

Junhui Wu<sup>ID</sup>, Cheng Yang, Zhenwang Luo, Xu Wang, Fei Zheng, Zhenfu Zhao, and Ziyang Hu<sup>ID\*</sup>

*Department of Microelectronic Science and Engineering, School of Physical Science and Technology, Ningbo University, Ningbo 315211, China*



(Received 6 April 2024; revised 2 June 2024; accepted 23 July 2024; published 14 August 2024)

The negative capacitance (NC) effect observed in perovskite-based devices is a unique phenomenon that remains subject to debate regarding its origin. In this study, we present a unified model aimed at describing these NC features, providing valuable insights into the coupling of ionic and electronic properties that give rise to NC behavior. Through meticulous analysis of impedance spectra, capacitance-frequency relationships, and current-voltage profiles under varying conditions of light intensity and bias voltage, we aim to uncover the underlying sources of NC in perovskite solar cells (PSCs). Our findings suggest that the emergence of NC in PSCs directly correlates with the migration of both positive and negative ions toward the uppermost and lowermost surfaces of the perovskite layer. Moreover, the polarity of capacitance at low frequencies is determined by the predominant recombination pathway within the device. We present a unified model that comprehensively describes the evolution of NC in PSCs. This model not only elucidates experimental observations but also confirms the connection between NC and recombination mechanisms.

DOI: 10.1103/PhysRevApplied.22.024041

## I. INTRODUCTION

The capacitance characteristics offer a nondestructive means to assess semiconductor devices and evaluate their structural and physical parameters. Capacitance or admittance spectra also provide crucial insights into device physics, aiding in the accurate interpretation of experimental data. Among these capacitance features, the phenomenon of negative capacitance (NC) is particularly noteworthy. Semiconductor devices often exhibit NC behavior in the low- or intermediate-frequency range during impedance spectroscopy measurements. The induction effect in transistors was reported as early as the 1960s [1] and, subsequently, NC effects have been observed in various electronic devices composed of crystals or amorphous semiconductors, including *p-n* junctions, Schottky diodes, and ferroelectric capacitors [2–5]. The microphysical mechanisms of NC behavior vary for different types of devices. Essentially, there are two distinct ways to explain NC behavior. For Schottky diodes or traditional *p-n* junctions, observed NC is often attributed to volume effects, wherein the injection of a large number of minority carriers under high-bias voltage reduces the serial resistance of the material [6,7]. Conversely, for organic semiconductor devices, NC observed at low frequencies is explained as a characteristic of sequential electron injection at the organic-metal interface [8–10]. However, the complex interplay of rich interface contacts, the mixed

ion-electron nature, and intrinsic chemical instability in perovskite-based devices complicate the measurement and interpretation of the observed NC behavior.

Several explanations of NC phenomena in perovskite-based devices have been proposed, including recombination at the perovskite interface [11–18], chemical and structural properties of the perovskite-contact interface [19–21], and vacancy-assisted ionic diffusion [22–24]. However, its physical origin has not been conclusively identified. The existing issues can be broadly categorized into the following aspects. First, the conditions for the appearance of NC in photovoltaic devices are not clear. Each layer of the device affects the NC behavior [19–21]. Second, the relationship between external bias conditions and the NC phenomenon under light excitation is unclear. The appearance of NC is confined to a specific voltage range [25]. Light significantly impacts capacitance, as illumination causes the disappearance of the NC phenomenon [14,16]. Third, the current theoretical framework lacks a comprehensive physical mechanism supported by empirical evidence. Although the NC effect can be accommodated within existing models to some extent [16,26], there is a scarcity of experimental data to validate these theoretical constructs.

In this work, we addressed the above issues by meticulously analyzing impedance spectra, capacitance-frequency relationships, and current-voltage profiles under diverse conditions of light intensity and bias voltage. Our aim is to unravel the underlying sources of NC in perovskite solar cells (PSCs). By utilizing a standard

\*Contact author: huziyang@nbu.edu.cn

coupled drift-diffusion model to simulate the motion of ions in perovskite, we have precisely predicted the conditions for the occurrence of NC and its correlation with the predominant recombination pathway affected by ion migration.

## II. EXPERIMENTAL DETAILS

The F-doped tin oxide (FTO) transparent conductive substrate is cleaned by ultrasonically washing it in deionized water, ethanol, deionized water, and ethanol for 15 min each, followed by ozone treatment for 10 min after drying. The PEDOT:PSS layer is prepared using a spin-coating method, with filtered PEDOT:PSS stock solution mixed with deionized water at a volume ratio of 1:3 and allowed to stand at 0 °C for 12 h. During spin-coating, after the rotation speed reaches 4000 rpm, two drops of PEDOT:PSS solution are pipetted, followed by spinning for 30 s and annealing at 150 °C in air for 15 min.

The MAPbI<sub>3</sub> thin film is prepared using a two-step spin-coating method, where 1 M Pb and methylammonium iodide (MAI) are dissolved in an organic solvent mixture of N,N-dimethylformamide (DMF) and dimethyl sulfoxide (DMSO) at a ratio of 7:3. After complete dissolution, 50 μL is uniformly dropped on the substrate, spun at 1000 rpm for 5 s and then at 2800 rpm for 30 s. In the second spin-coating step, after 10 s, 170 μL of chlorobenzene (CB) extract is uniformly pipetted and then annealed at 40 °C, 60 °C, 75 °C, and 85 °C for 5 min each in a gradient manner.

The [6,6]-Phenyl-C61-butyric acid methyl ester (PCBM) layer is prepared by dissolving 1M PCBM in CB, dropping two drops on the substrate, spinning at 2500 rpm for 30 s, and then annealing at 60 °C for 10 min. After annealing, the supernatant of the oversaturated bathocuproine (BCP) solution is taken, and after spinning at 5500 rpm for 30 s, annealing is performed at 50 °C for 5 min. Approximately 80 nm of silver contacts are thermally evaporated on the backside using a shadow mask with 0.24 rectangular holes.

For testing *J*–*V* curves, transient photocurrent, and impedance spectra, the multifunctional charge carrier mobility measurement system (PAIOS, Fluxim, Switzerland) is used, with illumination provided by a 15.2 mW/cm<sup>2</sup> LED white light. For the impedance spectroscopy measurements, an AC perturbation of 7 mV voltage is applied on a DC positive bias, which varies from 0 to 2 V, with an AC frequency ranging from 1 MHz to 10 Hz. The proposed equivalent circuit is fitted using ZSIMPPWIN software for spectral fitting.

## III. RESULTS AND DISCUSSION

For PSCs employing the ITO/PEDOT:PSS/MAPbI<sub>3</sub>/PC<sub>61</sub>BM/Ag structure, we designated a high power-conversion efficiency device lacking negative capacitance

(NC) as Device B, while a low power-conversion efficiency device exhibiting NC was labeled as Device A. The representative *J*–*V* curves of these devices are shown in Fig. S1 in the Supplemental Material [37]. Previous studies have highlighted the correlation between interfacial recombination and NC [11–18]. To further investigate this, we fabricated solar cells with the ITO/MAPbI<sub>3</sub>/PC<sub>61</sub>BM/Ag structure, omitting the hole transport layer (HTL), which is expected to enhance interfacial recombination. These cells are denoted as Device C; they also lack NC. Figure 1 illustrates the relationship between the capacitance (*C*) of the devices as a function of frequency and bias voltage, with the corresponding impedance spectra displayed in Fig. S2 in the Supplemental Material [37].

In the high-frequency regime (>10<sup>3</sup> Hz), the capacitance is primarily dominated by the geometric capacitance (*C*<sub>0</sub>) of the device, which depends on the thickness and material properties. Additionally, the depletion layer capacitance within the device contributes to the high-frequency capacitance, causing slight variations with changes in voltage and frequency. However, in the low-frequency region (<10<sup>3</sup> Hz), as depicted in Fig. 1(a), the capacitance of Device A starts to decline, eventually becoming negative. Additionally, as frequency decreases, NC increases, while the capacitance of Devices B and C sharply rises in Figs. 1(b) and 1(c). This indicates that the physical processes underlying the low-frequency capacitance are closely related to both voltage and frequency.

To elucidate the behavior of NC further, we analyzed data for these devices in the time domain. Transforming frequency-domain information of impedance spectra into the time domain through Fourier transformation enables a direct correlation between the NC effect and hysteresis in the *J*–*V* curve, akin to the general low-frequency response of the impedance [14,16,27,28]. As shown in Fig. 2, the *J*–*V* curves exhibit divergence in the forward and reverse directions, with the forward current exceeding the reverse current, indicating normal hysteresis, and the reverse current exceeding the forward current, suggesting inverted hysteresis [16]. In Fig. 2(a), the hysteresis of Device A transitions from normal to inverted as the scan rate decreases, which corresponds to the shift from high-frequency capacitance to low-frequency inductance observed in Fig. 1(a). In contrast, the hysteresis curve observed for Device B and C in Figs. 2(b) and 2(c), respectively, remain consistently normal, corresponding to the consistently positive capacitance values shown in Figs. 1(b) and 1(c). These characteristics are attributed to the slow ion transport effect [29,30]. Due to the significantly slower movement of ions compared with the response of electrons, the observed delay in current results in both capacitive and inductive components.

The low-frequency NC phenomenon can be complex and not always straightforward. Despite having

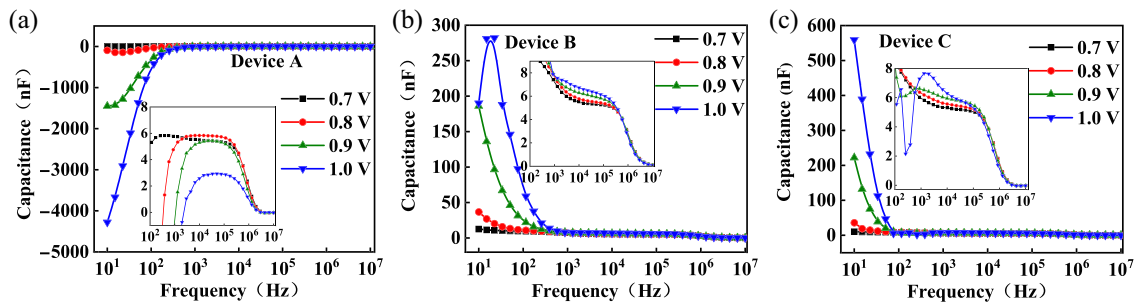


FIG. 1. Capacitance frequency ( $C$ – $F$ ) of (a) Device A, (b) Device B, and (c) Device C at different voltages.

the same architecture, Devices A and B exhibit opposite low-frequency capacitance behaviors. Atomic force microscopy measurements reveal that Device A has an average surface roughness of 8.9 nm, while Device B has a roughness of 12.0 nm (Fig. S3 in the Supplemental Material [37]). The increased surface roughness in Device B reduces charge transport across the perovskite layer interface, promoting more recombination [31]. In contrast, the smoother surface of Device A (8.9 nm) enhances the likelihood of forming a uniform and smooth interface with the HTL [32], providing a better foundation for improved electronic contact between the perovskite layer and the HTL [33,34]. The SEM images (Fig. S4 in the Supplemental Material [37]) also indicate that the surface of Device B is rougher and has more distinct grains compared with Device A. To further explore the relationship between these surface properties and the observed electrical behaviors, Fig. 3 provides a comparative analysis of the ideality factors for the three devices. Regarding the ideality factor  $n_{id}$ , according to the Shockley ideal diode equation ( $J_{dark}V = J_0(\exp(eV/n_{id}k_B T) - 1)$ ), for perovskite devices, a  $n_{id}$  value close to 1 indicates radiative recombination and surface nonradiative recombination, while a  $n_{id}$  value close to 2 indicates bulk nonradiative recombination [35,36] (see Supplemental Material [37]). In this study, we determined the ideality factor of the devices from the dark  $J$ – $V$  curves ( $n_{id} = (eJ_{dark}V/k_B T)(dV/dJ)$ ). The ideality factor

for Device A ( $n_{id} = 1.9$ ) is greater than for Device B ( $n_{id} = 1.21$ ) and Device C ( $n_{id} = 1.26$ ). This indicates that carrier recombination in Device A predominantly occurs through trap-assisted bulk recombination while, in Devices B and C, recombination is more inclined toward trap-assisted surface recombination.

For a more detailed analysis, we tested Device A under various conditions. Figure 4(a) shows the capacitance  $C$  variation in the dark state of Device A under elevated bias conditions. At a bias voltage of 0.8 V, low-frequency NC (1 kHz, 100 Hz) is observed, increasing with the bias voltage and peaking at 1.1 V. Beyond this threshold, NC decreases, and the capacitance at 1 kHz turns positive at 1.3 V, indicating the NC is confined to a specific voltage range. A similar behavior is observed in the impedance of Device A under illumination. As depicted in Figs. 4(b) and 4(c), under a fixed bias voltage of 0.9 V, the high-frequency capacitance of the device remains unaffected by varying light intensities, whereas the high-frequency resistance exhibits a decrease with increasing light intensity. Additionally, the NC in the low-frequency region disappears, and the low-frequency positive capacitance grows with increasing light intensity. The variation of resistance and capacitance with light intensity is illustrated in Fig. 4(d). The changes in impedance under illumination can be explained by the nonuniform distribution of photogenerated carriers [Fig. S6(b) in the Supplemental Material [37]] with the highest concentration occurring

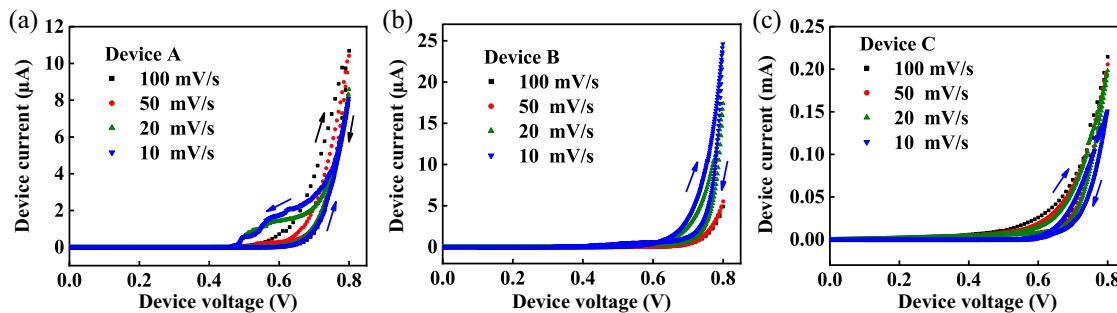


FIG. 2. Under dark conditions, the forward and reverse  $J$ – $V$  scans of (a) Device A, (b) Device B, and (c) Device C with different scan rates.

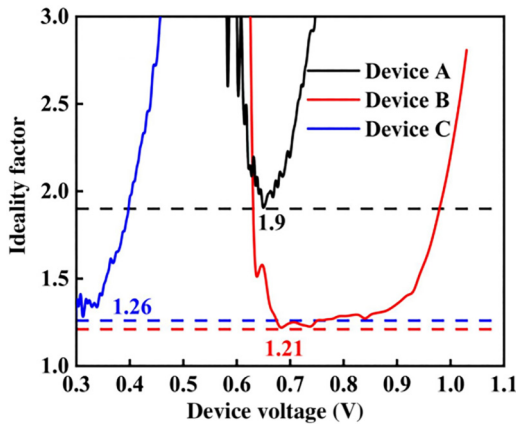


FIG. 3. Comparison of ideality factors for the devices.

at the interface. As the depth of the perovskite layer increases, the concentration of photogenerated carriers decreases exponentially. Moreover, with higher light intensities, there is a greater accumulation of photogenerated carriers at the interface. Similarly, the accumulation of interface charges can also account for the changes in low-frequency capacitance under high-bias voltages. At higher voltages, there is a significant increase in the injection of charges, leading to the formation of charge accumulation regions near the electrodes, thereby resulting in an increase in capacitance [25].

Based on the aforementioned observations, the gradual relaxation of ions is considered the underlying cause of low-frequency impedance characteristics. By analyzing representative devices labeled as Device A, B, and C, NC is found only in Device A, characterized by lower efficiency and bulk recombination acting as the dominant mechanism. Conversely, neither Device B, exhibiting higher efficiency, nor Device C, which lacks the hole transport layer to enhance surface recombination, exhibits NC. However, the NC in Device A is not fixed; under conditions of increased charge accumulation at the device interface (high bias or illumination), the NC effect diminishes and is replaced by low-frequency positive capacitance. This raises the possibility that NC originates from the modulation of bulk recombination current by ion migration, while ions induce low-frequency positive capacitance that affects surface recombination. This elucidates why negative capacitance is observed only in certain devices. The polarity of the low-frequency capacitance is determined by the prevailing recombination mechanism in the device at the current state.

The surface polarization model was previously proposed to explain NC [15,38] but, due to the complexities in actual measurements, some puzzling issues remain. One of the main assumptions of the surface polarization model is the distinction between the external voltage  $V(t)$  and the surface polarization voltage  $V_s$  under ion modulation [39].

In this study, we interpret this lag in surface voltage as a result of interfacial ion accumulation. As shown in Fig. 5, changes in the external voltage  $V(t)$  generate a bulk electric field  $E_{\text{bulk}}$ . This bulk electric field drives ions toward the interface, where they gradually screen  $E_{\text{bulk}}$ . The relaxation of  $E_{\text{bulk}}$  leads to the difference between  $V(t)$  and  $V_s$  ( $V(t) + V_{\text{bi}} = V_s + bE$ ).

The current through the device,  $J$ , can be divided into different components:

1. A displacement current,  $j_d$ , that represents the device as a geometric capacitor undergoing charging and discharging.
2. The remaining part of the current,  $j_{\text{rec}}$ , consisting of recombination currents based on the location of carrier recombination.
3. Recombination occurring at the interface that corresponds to the surface recombination current,  $j_{\text{rec}1}$ . Recombination occurring within the perovskite layer corresponds to the bulk recombination current,  $j_{\text{rec}2}$ .

The model equation is given by the following:

$$J = j_d + j_{\text{rec}}, \quad (1)$$

$$V + V_{\text{bi}} = V_s + bE. \quad (2)$$

The impedance is defined as

$$Z(\omega) = \frac{\hat{V}}{\hat{J}} = R + iX. \quad (3)$$

The rate of charge accumulation within the depletion layer following a voltage alteration is governed by the quantity of mobile ions. These ions migrate to the interface propelled by  $E_{\text{bulk}}$  during that specific timeframe so that

$$dQ = vqNdt = E_{\text{bulk}}qNdt. \quad (4)$$

where  $\mu$  is the ion migration rate,  $N$  is the ion concentration, and  $v$  is the velocity of ions driven by  $E_{\text{bulk}}$ . The depletion layer charge is related to the interfacial potential by the following functional relationship: [40]

$$Q(V_s) = \sqrt{qN\varepsilon_p V_T} \text{sign}(V_s) \sqrt{2} \left( e^{V_s/V_T} - \frac{V_s}{V_T} - 1 \right)^{1/2}. \quad (5)$$

By combining Eqs. (4) and (5), and replacing all the constant terms with  $\tau_0$ , i.e.,  $\tau_0 = \mu q N (dV_s/dQ)|_{V_s=\bar{V}_s}$ , we derive the following:

$$\tau_0 E_{\text{bulk}} = \frac{dV_s}{dt}, \quad (6)$$

for the surface potential perturbation term  $\hat{V}_s$ . Due to the generation of the bulk electric field,  $\hat{V}_s$  is no longer

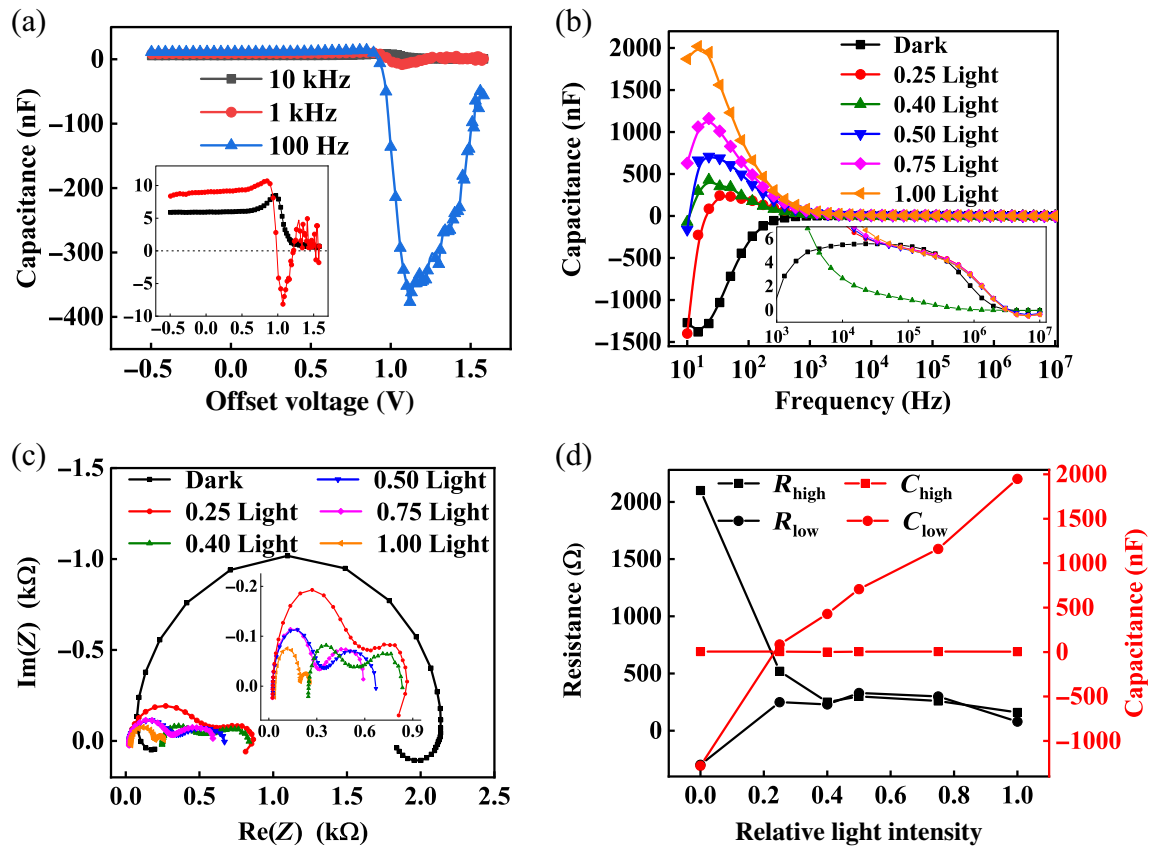


FIG. 4. (a)  $C$ - $V$  characteristics of Device A under different frequencies in the dark. (b)  $C$ - $F$  characteristics and (c) the impedance spectrum of Device A with a fixed bias voltage of 0.9 V under different light intensities. The power of the light is 15.2 mW/cm $^2$ . (d) Resistance and capacitance obtained by describing the electrochemical impedance spectroscopy (EIS) data measured in different light intensities.

directly equal to the variation in the applied voltage  $\hat{V}$ . After accounting for the contribution of  $E_{\text{bulk}}$ ,  $\hat{V}_s$  can be expressed as

$$\hat{V}_s = \hat{V} - bE. \quad (7)$$

By combining Eqs. (6) and (7), we determine that

$$\hat{V}_s = \frac{\hat{V}}{i\omega(b/\tau_0) + 1}. \quad (8)$$

Given the potential distribution in the perovskite material ( $V = V_1 + V_2 + xE$ ), assuming an electron concentration

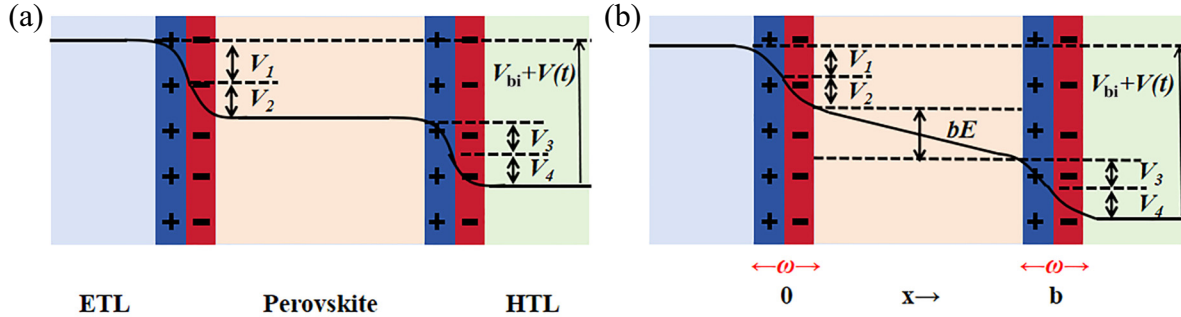


FIG. 5. (a) Potential distribution diagram of a perovskite solar cell under steady-state conditions. (b) Potential diagram when an external voltage changes, generating a bulk electric field. Here,  $V(t)$  and  $V_{\text{bi}}$  represent the applied voltage and the built-in voltage, respectively, and  $V_1$ ,  $V_2$ ,  $V_3$ , and  $V_4$  denote the voltages within the space charge region;  $V_s$  is the surface polarization voltage ( $V_s = V_1 + V_2 + V_3 + V_4$ ).

of  $n_0$  in the electron transport layer (ETL), the carrier concentration distribution in the device can be obtained as

$$n = n_0 \exp\left(-\frac{q(V_1 + xE)}{k_0 T}\right) \quad 0 \leq x \leq b. \quad (9)$$

For trap-assisted recombination (Shockley-Read-Hall recombination), when electron recombination is dominant, the recombination rate can be expressed as  $R \approx (np/\tau_p n + \tau_n p) \approx (n/\tau_n)$  [41–43]. Here,  $\tau_n$  represents the electron lifetime. The recombination current is given by  $j_{\text{rec}} = qRd$ , and the surface recombination current  $j_{\text{rec1}}$  and the bulk recombination current  $j_{\text{rec2}}$  can be expressed as follows:

$$j_{\text{rec1}} = qv_n n_0 \exp\left(-\frac{q(V_1 + V_2 + V_3 + bE)}{n_{\text{id}} k_0 T}\right), \quad (10)$$

$$j_{\text{rec2}} = \frac{qb n_0}{\tau_n} \exp\left(-\frac{2qV_1 + 2qV_2 + qbE}{n_{\text{id}} k_0 T}\right). \quad (11)$$

In these equations,  $n_{\text{id}}$  represents the ideality factor, where  $n_{\text{id}} = 1$  for surface recombination and  $n_{\text{id}} = 2$  for bulk recombination. By combining Eqs. (3)–(11), the impedance analytical expression for the model can be derived (see Supplemental Material [37]) as follows:

$$Z^{\text{eq}} = \left( \frac{1}{R_{L1} + R_{L2} + R_H} + i \frac{C_L}{\omega} - i \frac{L}{\omega} + i\omega C_H \right)^{-1}, \quad (12)$$

$$C_H = C_0, \quad (13)$$

$$R_H(V) = R_{H0} e^{-(V_{H0}/V)}, \quad (14)$$

$$C_L(V) = \left( 1 - \frac{\hat{V}_1 + \hat{V}_2 + \hat{V}_3}{\hat{V}_s} \right) C_{L0} e^{-(V/V_{L0})}, \quad (15)$$

$$R_{L1}(V) = \left( \frac{\hat{V}_s}{\hat{V}_1 + \hat{V}_2 + \hat{V}_3} - 1 \right) R_{L10} e^{-(V_{L0}/V)}, \quad (16)$$

$$L(V) = \left( \frac{\hat{V}_1 + \hat{V}_2}{\hat{V}_s} - \frac{1}{2} \right) L_0 e^{-(V/V_{L0})}, \quad (17)$$

$$R_{L2}(V) = \left( \frac{\hat{V}_s}{\hat{V}_1 + \hat{V}_2} - 2 \right)^{-1} R_{L20} e^{-(V/V_{L0})}. \quad (18)$$

Equations (13)–(18) demonstrate a robust correlation between the circuit components, enabling the derivation of

relaxation times for various physical processes so that

$$\tau_H = C_H R_H = \frac{n_{\text{id}} k_0 T}{q^2 v_n n_0} \exp\left(-\frac{k_0 T}{q} F(V)\right), \quad (19)$$

$$\tau_C = C_L R_{L1} = \alpha \frac{\tau_0^2}{b^2}, \quad (20)$$

$$\tau_L = -L/R_{L2} = \beta \frac{\tau_0^2}{b^2}. \quad (21)$$

The relaxation time  $\tau_H$  of the high-frequency component decreases exponentially with increasing voltage, whereas the slow relaxation process associated with the low-frequency component remains a voltage-independent constant. In these expressions,  $\alpha$  and  $\beta$  are recombination parameters, with  $\alpha$  denoting surface recombination

$$\begin{aligned} \left( 1 < \alpha = \left( 1 - \frac{\hat{V}_1 + \hat{V}_2 + \hat{V}_3}{\hat{V}_s} \right) \times \left( \frac{\hat{V}_s}{\hat{V}_1 + \hat{V}_2 + \hat{V}_3} - 1 \right) < 1.5 \right) \end{aligned}$$

and  $\beta$  denoting bulk recombination

$$\left( 0 < \beta = \left( \frac{1}{2} - \frac{\hat{V}_1 + \hat{V}_2}{\hat{V}_s} \right) \left( \frac{\hat{V}_s}{\hat{V}_1 + \hat{V}_2} - 2 \right) < 0.5 \right).$$

Figure 6 demonstrates a strong agreement between the relaxation times derived from experimental data and those calculated using Eqs. (20) and (21). This model successfully explains the temporal variation of the device's relaxation time  $\tau$ . Notably, the experimentally obtained slow relaxation time  $\tau_B$  for Device B is shorter than both the relaxation time  $\tau_A$  for Device A and the theoretical slow relaxation time  $\tau_L$  for the surface recombination current component. This discrepancy can be attributed to the fact that the slow relaxation time  $\tau$  is also closely linked to the ion concentration  $N$  in the device ( $\tau \propto \tau_0^2 \propto N^2$ ). Comparative analysis of the  $J$ – $V$  curves (Fig. S1 in the Supplemental Material [37]) and impedance spectra (Fig. S2 in the Supplemental Material [37]) reveals that Device B, which exhibits superior performance and fewer defect-related recombinations than Device A, has a lower ion concentration. As a result, the low-frequency characteristic time constant  $\tau_B$  is shorter than  $\tau_A$ .

The equivalent circuit is shown in Fig. 7. Here,  $C_H$  and  $R_H$  are the geometric capacitance and the composite resistance of the device, respectively;  $C_L$  and  $R_{L1}$  signify the phase and magnitude of the trap-assisted surface recombination current, which is modulated by ions. With both coefficients being positive, they contribute positively to the low-frequency capacitance and resistance;  $L$  and  $R_{L2}$  denote the impact of ion migration on the trap-assisted

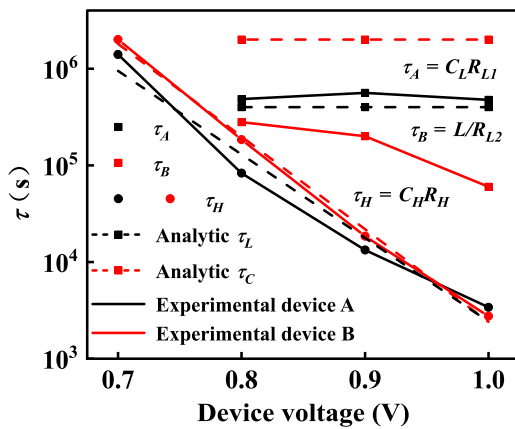


FIG. 6. Relaxation times derived from experimental data and analytical calculations. The parameters utilized for the analytical calculations include carrier charge  $q = 1.6 \times 10^{-19}$  C, recombination parameters  $\alpha = 0.25$ ,  $\beta = 1.25$ , perovskite layer thickness  $d = 400$  nm, ion concentration  $N = 2 \times 10^{20}$  cm $^{-3}$  [44], effective ion mobility  $\mu = 5 \times 10^{-11}$  m $^2$  V $^{-1}$  S $^{-1}$  [45], and the ratio of Debye layer voltage to charge  $dV_s/dQ|_{V_s=\bar{V}_s} = 5$  VC $^{-1}$  [46].

bulk recombination current. When the voltage perturbation at the ETL-perovskite interface ( $\hat{V}_1 + \hat{V}_2$ ) surpasses that at the perovskite-HTL interface ( $\hat{V}_3 + \hat{V}_4$ ), the coefficients become negative, resulting in negative values for the low-frequency capacitance and resistance. A constant series resistance ( $R_s$ ) represents losses in the external circuit. The fits effectively capture the features of the impedance spectra, as shown in Fig. 7, successfully reproducing the impedance spectrum characteristics discussed previously.

The dependency of  $C_L$  and  $R_L$  on voltage in the present devices exhibits exponential trends. At low voltages,  $C_L$  is predominantly determined by the  $C_0$  of the device. However, as the applied bias voltage approaches the device's open-circuit voltage, there is a pronounced increase in  $C_L$ , which can be attributed to the alterations in the charge carrier dynamics. This alteration readily accounts for the

abrupt changes observed in  $C_L$  at higher bias voltages. In Device B, which primarily exhibits surface recombination,  $C_L$  is large and we can obtain the double RC feature of Fig. 7(a). In device A, carrier recombination predominantly entails bulk recombination, resulting in a relatively large inductive component  $L$ . The capacitive arc is not observed at low frequencies and is replaced by the chemical inductor feature of Fig. 7(b).

The low-frequency impedance characteristics are determined by the primary recombination mechanism of the device. Under illumination, the recombination mechanism changes due to the nonuniform distribution of photogenerated carriers [Fig. S6(b) in the Supplemental Material [37]]. Consequently, the equivalent impedance reflecting the inductive and capacitive components in the impedance function is given by

$$Z_L^{\text{eq}} = \left( \exp\left(\frac{q(V_{L0} - ab)}{k_0 T}\right) \left( \frac{1}{R_{L2}} - i \frac{L}{\omega} \right) \right)^{-1}, \quad (22)$$

$$Z_C^{\text{eq}} = \left( \exp\left(\frac{qV_{L0}}{k_0 T}\right) \left( \frac{1}{R_{L1}} + i \frac{C_L}{\omega} \right) \right)^{-1}. \quad (23)$$

The accumulation of photogenerated carriers at the incident interface increases the interface recombination of carriers, leading to an increase in the capacitive component of the impedance function. Therefore, in our experiments, we observed a transition from low-frequency negative capacitance to positive capacitance under illumination. In addition, as the light intensity increases, the low-frequency capacitance continues to rise.

The origin of NC in PSCs using a unified model was investigated. Our analysis established the relationship between the NC effect, ion migration, and recombination mechanisms. In addition, we proposed a surface polarization model to quantitatively characterize this relationship. Experimental validation of the model confirms that both

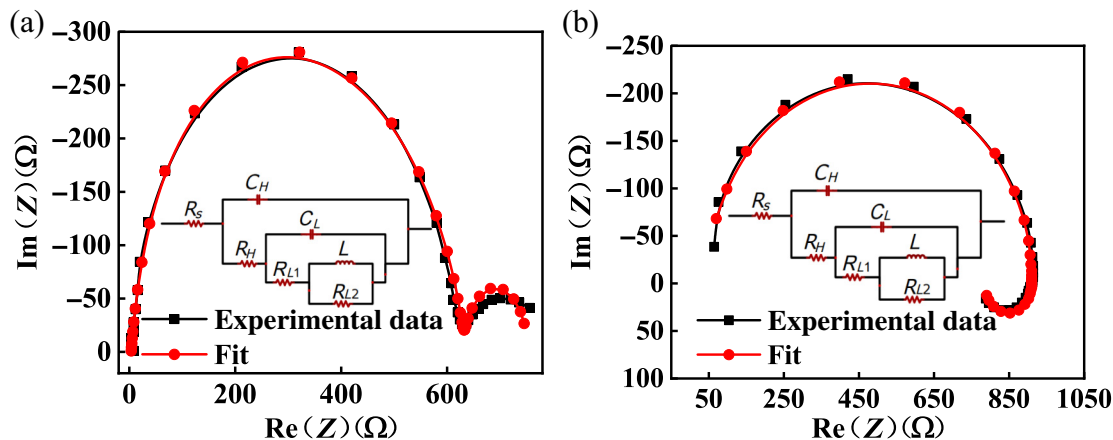


FIG. 7. (a) Experimental data and fitting curves for Device B and (b) experimental data and fitting curves for Device A.

illumination and bias voltage notably influence negative capacitance. This study provides valuable insights into the origin of NC and its association with carrier recombination mechanisms in PSCs.

#### IV. CONCLUSION

In summary, we have conducted a comprehensive analysis of impedance spectroscopy measurements across various solar cell architectures. Our research sheds light on the intricate relationship between the NC effect and fundamental carrier recombination mechanisms, particularly focusing on ion dynamics at both the surface and within the bulk of perovskite materials. By refining the surface polarization model, we have derived analytical expressions that quantitatively link the NC effect to carrier recombination processes. Our findings highlight the significant influence of illumination and bias voltage on modulating the NC effect, providing a succinct explanation for its dissipation under illuminated conditions. This model not only establishes a robust theoretical framework for optimizing the performance of perovskite-based devices but also offers a fresh perspective on carrier recombination dynamics.

#### ACKNOWLEDGMENTS

This work was supported by the National Natural Science Foundation of China (Grant Nos. 62074088, 62174094, 62304116), the Foundation of Zhejiang Educational Commission (Grant No. Y201737090), and the Ningbo S&T Innovation 2025 Major Special Programme (2018B10055). The author Z. Hu would like to thank the sponsorship by K.C. Wong Magna Fund in Ningbo University.

The authors declare no competing financial interest.

- [1] J. Lindmayer and W. North, The inductive effect in transistors, *Solid-State Electron.* **8**, 409 (1965).
- [2] B. Jones, J. Santana, and M. McPherson, Negative capacitance effects in semiconductor diodes, *Solid State Commun.* **107**, 47 (1998).
- [3] A. I. Khan, K. Chatterjee, B. Wang, S. Drapcho, L. You, C. Serrao, S. R. Bakaul, R. Ramesh, and S. Salahuddin, Negative capacitance in a ferroelectric capacitor, *Nat. Mater.* **14**, 182 (2015).
- [4] T. Misawa, Negative resistance in pn junctions under avalanche breakdown conditions, Part I, *IEEE Trans. Electron Devices* **1**, 137 (1966).
- [5] X. Wu, E. Yang, and H. Evans, Negative capacitance at metal-semiconductor interfaces, *J. Appl. Phys.* **68**, 2845 (1990).
- [6] S. E. Laux and K. Hess, Revisiting the analytic theory of pn junction impedance: Improvements guided by computer simulation leading to a new equivalent circuit, *IEEE Trans. Electron Devices* **46**, 396 (1999).
- [7] J. Van Den Biesen, Modelling the inductive behaviour of short-base pn junction diodes at high forward bias, *Solid-State Electron.* **33**, 1471 (1990).
- [8] J. Bisquert, A variable series resistance mechanism to explain the negative capacitance observed in impedance spectroscopy measurements of nanostructured solar cells, *Phys. Chem. Chem. Phys.* **13**, 4679 (2011).
- [9] J. Bisquert, G. Garcia-Belmonte, Á. Pitarch, and H. J. Bolink, Negative capacitance caused by electron injection through interfacial states in organic light-emitting diodes, *Chem. Phys. Lett.* **422**, 184 (2006).
- [10] E. Ehrenfreund, C. Lungenschmied, G. Dennler, H. Neugebauer, and N. Sariciftci, Negative capacitance in organic semiconductor devices: Bipolar injection and charge recombination mechanism, *Appl. Phys. Lett.* **91**, 1 (2007).
- [11] J. Bisquert, Electrical charge coupling dominates the hysteresis effect of halide perovskite devices, *J. Phys. Chem. Lett.* **14**, 1014 (2023).
- [12] J. Bisquert, A. Guerrero, and C. Gonzales, Theory of hysteresis in halide perovskites by integration of the equivalent circuit, *ACS Phys. Chem. Au* **1**, 25 (2021).
- [13] H. Dhifaoui, N. H. Hemasiri, W. Aloui, A. Bouazizi, S. Kazim, and S. Ahmad, An approach to quantify the negative capacitance features in a triple-cation based perovskite solar cells, *Adv. Mater. Interfaces* **8**, 2101002 (2021).
- [14] F. Ebadi, N. Taghavinia, R. Mohammadpour, A. Hagfeldt, and W. Tress, Origin of apparent light-enhanced and negative capacitance in perovskite solar cells, *Nat. Commun.* **10**, 1574 (2019).
- [15] E. Ghahremanirad, A. Bou, S. Olyaei, and J. Bisquert, Inductive loop in the impedance response of perovskite solar cells explained by surface polarization model, *J. Phys. Chem. Lett.* **8**, 1402 (2017).
- [16] C. Gonzales, A. Guerrero, and J. Bisquert, Transition from capacitive to inductive hysteresis: A neuron-style model to correlate I–V curves to impedances of metal halide perovskites, *J. Phys. Chem. C* **126**, 13560 (2022).
- [17] A. Guerrero, G. Garcia-Belmonte, I. Mora-Sero, J. Bisquert, Y. S. Kang, T. J. Jacobsson, J.-P. Correa-Baena, and A. Hagfeldt, Properties of contact and bulk impedances in hybrid lead halide perovskite solar cells including inductive loop elements, *J. Phys. Chem. C* **120**, 8023 (2016).
- [18] M. T. Khan, P. Huang, A. Almohammed, S. Kazim, and S. Ahmad, Mechanistic origin and unlocking of negative capacitance in perovskites solar cells, *IScience* **24**, 2 (2021).
- [19] L. Cojocaru, S. Uchida, P. V. Jayaweera, S. Kaneko, H. Wang, J. Nakazaki, T. Kubo, and H. Segawa, Effect of TiO<sub>2</sub> surface treatment on the current–voltage hysteresis of planar-structure perovskite solar cells prepared on rough and flat fluorine-doped tin oxide substrates, *Energy Technol.* **5**, 1762 (2017).
- [20] Q. Dong, M. Wang, Q. Zhang, F. Chen, S. Zhang, J. Bian, T. Ma, L. Wang, and Y. Shi, Discontinuous SnO<sub>2</sub> derived blended-interfacial-layer in mesoscopic perovskite solar cells: Minimizing electron transfer resistance and improving stability, *Nano Energy* **38**, 358 (2017).
- [21] T. W. Kim, M. Kim, L. Cojocaru, S. Uchida, and H. Segawa, Direct observation of the tunneling phenomenon in

- organometal halide perovskite solar cells and its influence on hysteresis, *ACS Energy Lett.* **3**, 2743 (2018).
- [22] V. W. Bergmann, Y. Guo, H. Tanaka, I. M. Hermes, D. Li, A. Klasen, S. A. Bretschneider, E. Nakamura, R. d. Berger, and S. A. Weber, Local time-dependent charging in a perovskite solar cell, *ACS Appl. Mater. Interfaces* **8**, 19402 (2016).
- [23] K. Domanski, B. Roose, T. Matsui, M. Saliba, S.-H. Turren-Cruz, J.-P. Correa-Baena, C. R. Carmona, G. Richardson, J. M. Foster, and F. De Angelis, Migration of cations induces reversible performance losses over day/night cycling in perovskite solar cells, *Energy Environ. Sci.* **10**, 604 (2017).
- [24] A. Kovalenko, J. Pospisil, O. Zmeskal, J. Krajcovic, and M. Weiter, Ionic origin of a negative capacitance in lead halide perovskites, *Phys. Status Solidi RRL* **11**, 1600418 (2017).
- [25] Q. Niu, N. I. Crăciun, G.-J. A. Wetzelaeer, and P. W. Blom, Origin of negative capacitance in bipolar organic diodes, *Phys. Rev. Lett.* **120**, 116602 (2018).
- [26] E. Hernández-Balaguera, B. Arredondo, C. Pereyra, and M. Lira-Cantú, Parameterization of the apparent chemical inductance of metal halide perovskite solar cells exhibiting constant-phase-element behavior, *J. Power Sources* **560**, 232614 (2023).
- [27] J. Bisquert, Inductive and capacitive hysteresis of current-voltage curves: Unified structural dynamics in solar energy devices, memristors, ionic transistors, and bioelectronics, *PRX Energy* **3**, 011001 (2024).
- [28] K. Dey, D. Ghosh, M. Pilot, S. R. Pering, B. Roose, P. Deswal, S. P. Senanayak, P. J. Cameron, M. S. Islam, and S. D. Stranks, Substitution of lead with tin suppresses ionic transport in halide perovskite optoelectronics, *Energy Environ. Sci.* **17**, 760 (2024).
- [29] V. M. Le Corre, J. Diekmann, F. Peña-Camargo, J. Thiesbrummel, N. Tokmoldin, E. Gutierrez-Partida, K. P. Peters, L. Perdigón-Toro, M. H. Futscher, and F. Lang, Quantification of efficiency losses due to mobile ions in perovskite solar cells via fast hysteresis measurements, *Sol. RRL* **6**, 2100772 (2022).
- [30] J. Thiesbrummel, S. Shah, E. Gutierrez-Partida, F. Zu, F. Peña-Camargo, S. Zeiske, J. Diekmann, F. Ye, K. P. Peters, and K. O. Brinkmann, Ion-induced field screening as a dominant factor in perovskite solar cell operational stability, *Nat. Energy* **9**, 1 (2024).
- [31] N. Mohammadian, A. Moshaii, A. Alizadeh, S. Gharibzadeh, and R. Mohammadpour, Influence of perovskite morphology on slow and fast charge transport and hysteresis in the perovskite solar cells, *J. Phys. Chem. Lett.* **7**, 4614 (2016).
- [32] Y. Lei, Y. Xu, M. Wang, G. Zhu, and Z. Jin, Origin, influence, and countermeasures of defects in perovskite solar cells, *Small* **17**, 2005495 (2021).
- [33] X. Shi, R. Chen, T. Jiang, S. Ma, X. Liu, Y. Ding, M. Cai, J. Wu, and S. Dai, Regulation of interfacial charge transfer and recombination for efficient planar perovskite solar cells, *Sol. RRL* **4**, 1900198 (2020).
- [34] D. Yang, X. Zhou, R. Yang, Z. Yang, W. Yu, X. Wang, C. Li, S. (Frank) Liu, and R. P. H. Chang, Surface optimization to eliminate hysteresis for record efficiency planar perovskite solar cells, *Energy Environ. Sci.* **9**, 3071 (2016).
- [35] W. Tress, M. Yavari, K. Domanski, P. Yadav, B. Niesen, J. P. C. Baena, A. Hagfeldt, and M. Graetzel, Interpretation and evolution of open-circuit voltage, recombination, ideality factor and subgap defect states during reversible light-soaking and irreversible degradation of perovskite solar cells, *Energy Environ. Sci.* **11**, 151 (2018).
- [36] P. Calado, D. Burkitt, J. Yao, J. Troughton, T. M. Watson, M. J. Carnie, A. M. Telford, B. C. O'Regan, J. Nelson, and P. R. Barnes, Identifying dominant recombination mechanisms in perovskite solar cells by measuring the transient ideality factor, *Phys. Rev. Appl.* **11**, 044005 (2019).
- [37] See Supplemental Material at <http://link.aps.org/supplemental/10.1103/PhysRevApplied.22.024041> for additional details on the analyses.
- [38] J. Bisquert, Hysteresis, impedance, and transients effects in halide perovskite solar cells and memory devices analysis by neuron-style models, *Adv. Energy Mater.* **14**, 2400442 (2024).
- [39] S. Ravishankar, O. Almora, C. Echeverría-Arondo, E. Ghahremanirad, C. Aranda, A. Guerrero, F. Fabregat-Santiago, A. Zaban, G. García-Belmonte, and J. Bisquert, Surface polarization model for the dynamic hysteresis of perovskite solar cells, *J. Phys. Chem. Lett.* **8**, 915 (2017).
- [40] O. Almora, C. Aranda, and G. García-Belmonte, Do capacitance measurements reveal light-induced bulk dielectric changes in photovoltaic perovskites?, *J. Phys. Chem. C* **122**, 13450 (2017).
- [41] D. W. de Quilettes, S. M. Vorpahl, S. D. Stranks, H. Nagaoka, G. E. Eperon, M. E. Ziffer, H. J. Snaith, and D. S. Ginger, Impact of microstructure on local carrier lifetime in perovskite solar cells, *Science* **348**, 683 (2015).
- [42] J. Huang, Y. Yuan, Y. Shao, and Y. Yan, Understanding the physical properties of hybrid perovskites for photovoltaic applications, *Nat. Rev. Mater.* **2**, 1 (2017).
- [43] D. Luo, R. Su, W. Zhang, Q. Gong, and R. Zhu, Minimizing non-radiative recombination losses in perovskite solar cells, *Nat. Rev. Mater.* **5**, 44 (2020).
- [44] A. Walsh, D. O. Scanlon, S. Chen, X. Gong, and S. H. Wei, Self-regulation mechanism for charged point defects in hybrid halide perovskites, *Angew. Chem.* **127**, 1811 (2015).
- [45] M. García-Batlle, S. Deumel, J. E. Huerdler, S. F. Tedde, O. Almora, and G. García-Belmonte, Effective ion mobility and long-term dark current of metal halide perovskites with different crystallinities and compositions, *Adv. Photonics Res.* **3**, 2200136 (2022).
- [46] N. E. Courtier, J. M. Cave, J. M. Foster, A. B. Walker, and G. Richardson, How transport layer properties affect perovskite solar cell performance: insights from a coupled charge transport/ion migration model, *Energy Environ. Sci.* **12**, 396 (2019).